# Using 1-Hz GPS Data to Measure Deformations Caused by the Denali Fault Earthquake

Kristine M. Larson, *et al.*

*Science* **300**, 1421 (2003);
DOI: 10.1126/science.1084531

oversampling ratio of $\sigma = S_{FFT}/S_{object} \approx 9$ (the FFT size was 1024 pixels by 1024 pixels), which is much higher than the $\sigma \geq 2$ condition required for the unique 2D reconstruction (*7*).

The reconstructed image of the double-wall carbon nanotubes from the experimental NAED pattern of Fig. 1B is shown in Fig. 2 (left). Inspection confirms that it is a double-wall tube. The fact that wall spacing is about the same on both sides provides direct support for the concentric tube model (*22*). By examining the image intensity profile, we measured the diameter of the outer wall as $D_1 = 4.04(1)$ nm; the inner wall, $D_2 = 3.33(1)$ nm; and the distance between two walls of the nanotube, $d = 0.35(1)$ nm. Most importantly, the hexagonal structure of the carbon sheet can be seen directly at localized areas. The accurate carbon nanotube diameters obtained from the image, coupled with the measurement of chiral angles from the diffraction pattern (*23*), allow a determination of the DWNT structure. The chiral vectors are (35, 25) and (26, 24) for the outer and inner tube, respectively. The two tubes are incommensurate with each other with a difference of 4.2° in helical angles. Figure 2 (right) offers a structure model for this DWNT. In projection, the overlap of four graphite layers creates Moiré fringes, which we see in our image (marked by parallel lines). There are areas of accidental coincidence where the graphite sheets align with each other. In each area, the carbon atoms are clearly resolved in the image (marked by hexagons). The carbon bond length is 1.42 Å, and features on the carbon nanotube walls are resolved with a resolution of 1 Å (*24*). All of these results support the structural model of two incommensurate, concentric, helical tubes.

We anticipate that the ability to record single-molecule diffraction with the use of NAED and the ability to reconstruct the image will find a wide range of applications in structure determinations of nonperiodic objects, from inorganic nanostructures to biological macromolecules. Because electrons interact with matter $\sim 10^4$ times more strongly than x-rays, single molecule diffraction, as we show here, can be carried out with the use of available electron sources. The resolution is diffraction intensity–limited. For radiation sensitive samples, including most biological molecules, the resolution will be limited by the amount of diffraction information that can be recorded below the radiation damage threshold. The threshold for macromolecule imaging is $\sim$ 10 e Å$^{-2}$ (*4*). For the 50-nm-long DWNT, an electron dose of $\sim 10^3$ e Å$^{-2}$ was needed for diffraction information at 1-Å resolution. The electron dose that a macromolecule with a large molecular weight will require will be less. Cryogenic cooling can also raise the radiation limit. Compared to the widely used phase-contrast imaging for biological samples, diffraction patterns record high-frequency structural information that is not limited by lens aberration and that has a large signal-to-noise ratio for structures with a high degree of order, such as carbon nanotubes. Both are favorable factors for the use of NAED for high-resolution imaging (*25*).

### References and Notes


1. J. C. H. Spence, *Science* **299**, 839 (2003).
2. C. L. Jia, M. Lentzen, K. Urban, *Science* **299**, 870 (2003).
3. M. A. O'Keefe *et al*., *Ultramicroscopy* **89**, 215 (2001).
4. R. Henderson, *Q. Rev. Biophys*. **28**, 171 (1995).
5. DWNT synthesis and observation are described on *Science* Online.
6. D. Sayre, *Acta Crystallogr. A* **5**, 843 (1952).
7. R. Bates, *Optik* **61**, 247 (1982).
8. R. P. Millane, *J. Opt. Soc. Am. A* **7**, 394 (1990).
9. J. Miao, P. Charalambous, J. Kirz, D. Sayre, *Nature* **15**, 342 (1999).
10. R. W. Gerchberg, W. O. Saxton, *Optik* **35**, 237 (1972).
11. J. Fienup, *Appl. Opt*. **21**, 2758 (1982).
12. R. P. Millane, W. J. Stroud, *J. Opt. Soc. Am. A* **14**, 568 (1997).
13. S. Iijima, *Nature* **354**, 56 (1991).
14. A. Jorio *et al*., *Phys. Rev. Lett*. **86**, 1118 (2001).
15. C. Dekker, *Phys. Today* **52**, 22 (1999).
16. J. Miao *et al*., *Phys. Rev. Lett*. 89, 155502 (2002). A focused electron beam was proposed for oversampling the electron diffraction pattern in the reported computational experiment. The beam convergence then limits the smallest sampling frequency.
17. The original pattern has a strong central peak and background from aperture scattering. We removed them by subtracting a diffraction pattern recorded without the tube. This results in an area of 60 pixels by 60 pixels with missing intensity. To fill this gap, we use the amplitude of Fourier transform of a low-resolution electron image.
18. The illuminating electron wave has the form of

$$\phi(\mathbf{r}) = \int_{-\infty}^{\infty} A(\mathbf{k}_\parallel) \exp\left[ i\pi k_\parallel^2 \lambda \left( \frac{C_s \lambda^2}{2} k_\parallel^2 + \Delta f \right) \right] \exp(2\pi i \mathbf{k}\cdot\mathbf{r}) d\mathbf{k}_\parallel$$

Here, $C_s$ and $\Delta f$ are the spherical aberration and the defocus of the electron lens, respectively. $A(\mathbf{k}_\parallel)$ has two components, a sharp peak on a broad background. Both can be modeled as a Gaussian function. The Gaussian half width of the sharp peak is $\sim$ 0.05 mrad, which can be approximated as a plane wave illumination.
19. I. A. Vartanyants, I. K. Robinson, *J. Phys. Condens. Matter* **13**, 10593 (2001).
20. J. C. H. Spence, U. Weierstall, M. Howells, *Philos. Trans. R. Soc. London Ser. A* **360**, 875 (2002).
21. We used the following constraints: In reciprocal space, the calculated amplitude on each iteration step was replaced by the measured Fourier amplitude $(I_{exp})^{1/2}$, keeping the phases. After the first $\sim$50 iterations, the central part of the diffraction pattern (60 pixels by 60 pixels) was allowed to vary without any constraint (only the high-resolution diffraction image was then used in these steps). In real space, the most important constraints for reconstruction of the electron interaction potential $U(\mathbf{r})$ are that the image has to be real and positive. We used the $R$ factor defined by $R = \Sigma \| F^{exp} | - | F^{Fit} \| / \Sigma | F^{exp} |$ to monitor the convergence of phase retrieval iterations. The best fit was selected from images with the lowest $R$.
22. In the image, one side of the DWNT is much sharper than the other. This effect comes partly from the variations in the projected potential along the wall and partly from an effect we attribute to a nonuniform illumination in the TEM.
23. M. Gao *et al*., *Appl. Phys. Lett*. **82**, 2703 (2003).
24. The nominal microscope point resolution is 2.2 Å for normal imaging at the Scherzer focus conditions, with $C_s$ = 1 mm and wavelength of 0.025 Å for the JEOL2010F microscope operated at 200 kV.


25. Work on electron microscopy characterization was supported by DOE DEFG02-01ER45923 and DEFG02-91ER45439 and the TEM facility of Center for Microanalysis of Materials at the Frederick Seitz Materials Research Laboratory. We thank J. H. Weaver, I. Robinson, S. Granick, R. Twesten, I. Petrov, R. Tsui, and H. Goronkin for discussion and encouragement.


**Supporting Online Material**

www.sciencemag.org/cgi/content/full/300/5624/1419/DC1
Materials and Methods
SOM Text
Fig. S1

26 February 2003; accepted 16 April 2003

# Using 1-Hz GPS Data to Measure Deformations Caused by the Denali Fault Earthquake

**Kristine M. Larson,[1]* Paul Bodin,[2] Joan Gomberg[3]**

**The 3 November 2002 moment magnitude 7.9 Denali fault earthquake generated large, permanent surface displacements in Alaska and large-amplitude surface waves throughout western North America. We find good agreement between strong ground-motion records integrated to displacement and 1-hertz Global Positioning System (GPS) position estimates collected $\sim$140 kilometers from the earthquake epicenter. One-hertz GPS receivers also detected seismic surface waves 750 to 3800 kilometers from the epicenter, whereas these waves saturated many of the seismic instruments in the same region. High-frequency GPS increases the dynamic range and frequency bandwidth of ground-motion observations, providing another tool for studying earthquake processes.**

Our understanding of how faults rupture during major earthquakes is limited by our observational capabilities; they also limit our understanding of the resulting ground deformation. Within a distance range of about the same dimension as the fault rupture (the near field), the surface deformation pattern is composed of a highly spatially variable permanent strain field generated by permanent displacements across the fault surface (coseismic offsets). These displacements form within tens of seconds and are superimposed on transient defor-

mations generated by oscillating seismic waves that may be observed globally for large earthquakes. Traditionally, accelerometers and seismometers record rapid movements of the Earth that occur on time scales of seconds. Accelerometers record the strongest near-field ground motions (measuring accelerations), and seismometers record more distant seismic waves (measuring velocities). GPS receivers, in contrast, record much slower displacements of the Earth that develop over days to years. For example, the slow, persistent uplift of a volcanic edifice due to magma influx or motion of tectonic plates can be measured with high resolution using GPS receivers (*1*).

A GPS receiver determines position instantaneously—but imprecisely—by measuring the distance between the receiver and four or more satellites. By tracking the GPS constellation over a 24-hour period, horizontal precisions of 2 to 4 mm can be achieved (*2*, *3*). Although many GPS receivers can operate at 1 to 10 Hz, most geophysicists record measurements at 0.033 Hz. In the past year, a growing number of continuously operating GPS receivers have increased their recording rates to 1 Hz to support missions in low Earth orbit (e.g., Gravity Recovery and Climate Experiment and Challenging Minisatellite Payload). Surveyors seeking solutions in real time also operate their receivers at 1 Hz. Here we examine whether 1-Hz GPS receivers can be used to measure near-field deformation and seismic waves radiated by the Denali fault earthquake.

The moment magnitude ($M$) 7.9 Denali fault earthquake ruptured the Susitna Glacier–Denali-Totschunda fault system on 3 November 2002 (*4*). This earthquake was complex, with an $M$ = 7.0 thrust subevent followed by an $M$ = 7.9 strike-slip event that ruptured to the east. Based on distant seismic recordings, the estimates of fault displacements at depth reach ~12 m. One-Hz GPS receiver data were collected from stations in Fairbanks (FAIR), Anchorage (TSEA), and Skagway (TEM1) in Alaska and from stations in Washington (BREW), Montana (MSOL), Colorado (AMC2), California (GOLD), and Maryland (GODE) (*5*) (Fig. 1). One-Hz GPS data are sensitive to the satellite constellation, both its geometry in the sky and the number of satellites in view. If the geometry of the constellation in the sky is poor, one component may be better determined than the other. This is the case with FAIR, the site closest to the epicenter. At the time of the earthquake, the satellites were lined up in a way that leads to precise longitude determinations but poor latitude determinations (Fig. 1, left inset). For comparison, the visible satellites at BREW are also shown. In general, height is more poorly determined by GPS than is the horizontal position.

We analyzed and compared the near-field deformation recorded at FAIR with some near-field seismic data. A recent study compared GPS and accelerograph data from the Hector Mine earthquake, but GPS sampling rates of 30 s limited its conclusions (*6*). The comparison we make is complicated somewhat by the fact that FAIR is ~20 km from the nearest seismic station and almost 140 km from the epicenter. Accelerograms from Fairbanks (station 8022 at 64.8735°N, 147.8614°W; Kinemetrics K2 instrumentation) were integrated twice to produce displacement time histories. Accelerographs have flat responses to acceleration and are operated primarily to record large-amplitude, high-frequency (1 Hz) accelerations for engineering analyses. Integration to determine a displacement time history, which constrains the coseismic offset at depth, is inherently an underdetermined problem and magnifies low-frequency noise. Thus, we high-pass filtered the acceleration measurements to remove long-term drift (cutoff period of 40 s) and then constrained the integration to agree with surface coseismic displacements (*4*) (Fig. 2).

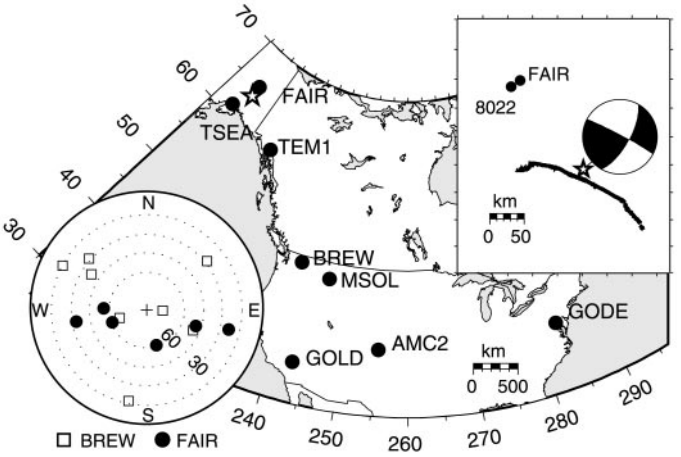


**Fig. 1.** Location of the Denali fault earthquake epicenter (star) along with 1-Hz GPS sites used in this study. The inset on the right shows the surface fault rupture, locations of FAIR and 8022, and the Harvard centroid moment tensor (CMT) focal mechanism for the earthquake. (*12*). The inset on the left shows the satellite constellation geometry at the time of the earthquake for FAIR and BREW. The azimuth directions are north, east, south, and west; elevation angles of the satellites are given by the concentric circles, spaced evenly between 15° and 60°. The center of the plot corresponds to the time when the satellite is directly overhead (elevation angle of 90°).

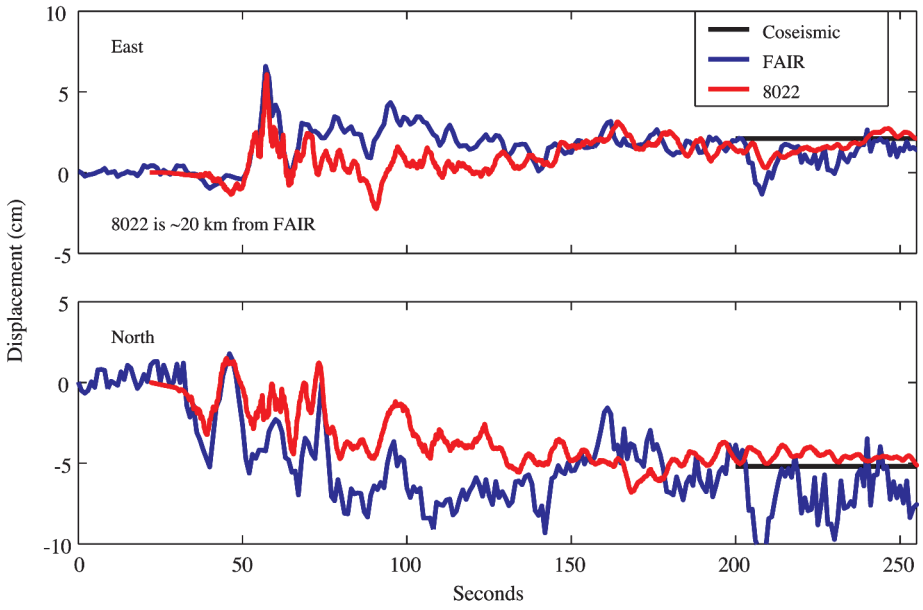


**Fig. 2.** Integrated seismic accelerations for station 8022 compared with 1-Hz GPS positions for FAIR. Time is relative to 3 November 2002 22:12:41 UTC. The integration was constrained to agree with the GPS-measured surface coseismic displacement. The coseismic displacements are derived by averaging the coordinates of FAIR 4 days before and after the earthquake (*4*). The 8022 observations were shifted by 3 s.

[1]Department of Aerospace Engineering Sciences, University of Colorado, Boulder, CO 80309–0429, USA. [2]Center for Earthquake Research and Information, University of Memphis, Memphis, TN 38152, USA. [3]U.S. Geological Survey, Memphis, TN 38152, USA.

*To whom correspondence should be addressed. E-mail: kristine.larson@colorado.edu

The 20-km separation between FAIR and seismic instruments and the dispersive nature of the large-amplitude seismic surface waves mean that the two types of records will be out of phase. Nevertheless, the agreement between the records is marked. The difference in noise characteristics of the east and north GPS records, most apparent before the arrival of the seismic signal, reflects the satellite geometry (Fig. 1). Although there is still a long-period discrepancy between the GPS data and seismic data, it is clear from this example that 1-Hz GPS instruments can capture the complete ground-motion time history during large earthquakes, thus providing insights into fundamental fault-propagation mechanisms. Moreover, such instruments provide a means of measuring static displacement offsets that is less sensitive to noise contamination than are seismic data. Accelerometer noise level may be related to the amplitude of the signal. For example, close to the rupture, tilting of the ground surface locally beneath the accelerometer may become large, and the accelerometer cannot distinguish between rotations and linear accelerations. However, close to the rupture, the GPS noise level should be the same as that at more remote sites, whereas the signal would increase to about half the fault slip (as much as 4 m for the Denali fault rupture).

Although signals from large earthquakes are now routinely recorded on high–dynamic range, broad-bandwidth seismometers, the Denali fault earthquake signal amplitudes still exceeded the recording capabilities out to distances of thousands of km (*7*). The largest amplitude waves beyond the near field are dispersive surface waves, with frequencies between ~1 and 0.01 Hz and group velocities of ~1 to 4 km/s. Our comparison of seismic and geodetic records indicates that GPS can be used to measure these seismic waves without the saturation problems of the seismometers. The east and north component records from TEM1, BREW, MSOL, AMC2, and GOLD show displacements beyond the distance of any detectable permanent coseismic deformation (Fig. 3).

The GPS data record the arrival of surface waves at distances as far as 3800 km (AMC2). Notably, the GPS records at TEM1 are on scale, whereas the more distant broadband seismic recordings at a seismometer (station DLBC at 58.437°N, 130.027°W) almost 300 km farther from the earthquake epicenter are clipped. Such observations are key for studying the focusing of waves due to rupture directivity and dynamic earthquake source processes. Our results, for example, show larger ground motions in the direction of rupture propagation and expected strongest directivity (along a great-circle path roughly through MSOL and AMC2), relative to motions at GOLD that are the same magnitude as the measurement noise. Such observations also are critical for interpreting the pattern of remotely triggered seismicity (*8*).

Our results demonstrate that GPS provides another important tool for studying earthquakes. Specifically, we show that GPS can resolve displacement changes that vary on time scales of seconds. For several types of measurements key to earthquake studies, GPS offers several advantages over seismic instrumentation. Estimation of earthquake-generated coseismic offsets and strain fields requires measurement of ground displacements. The processing required to estimate these from seismic data inherently enhances noise. In GPS, displacements are the basic measurement and, thus, estimates do not suffer from this noise source. In addition, seismic wave amplitudes vary over many orders of magnitude and, although the dynamic ranges of the best seismometers can capture most of these, many saturate for the largest—and most interesting—earthquakes. The accuracy of GPS data actually improves as the magnitude increases and there is no saturation. Ultimately, quantitative assessment of the accuracy of both seismic and GPS measurements will require data to be recorded at the same location. Of the sites shown in Fig. 3, only GOLD has a nearby seismometer (station GSC, at 35.302°N, 116.806°W, ~15 km from GOLD). Even though the signal is smallest at GOLD, there is still considerable agreement between the seismic data and the GPS data (fig. S2). At greater distances it becomes difficult to separate differences in waveforms associated with local geologic structure and radiation pattern from those due to measurement imprecision.

These results also suggest an interesting, although not yet realized, possibility for measuring temporally and spatially rapidly varying strains associated with seismic waves, which can cause ground failure and certain types of structural damage. Differenced displacement data recorded by high–sample rate GPS receivers deployed as arrays with apertures on the order of hundreds of meters or less (fractions of seismic wavelengths) would provide direct strain measurements. These could be deployed both in the field for studies of earthquake processes and within built structures for engineering studies. Attempts to make such measurements with integrated

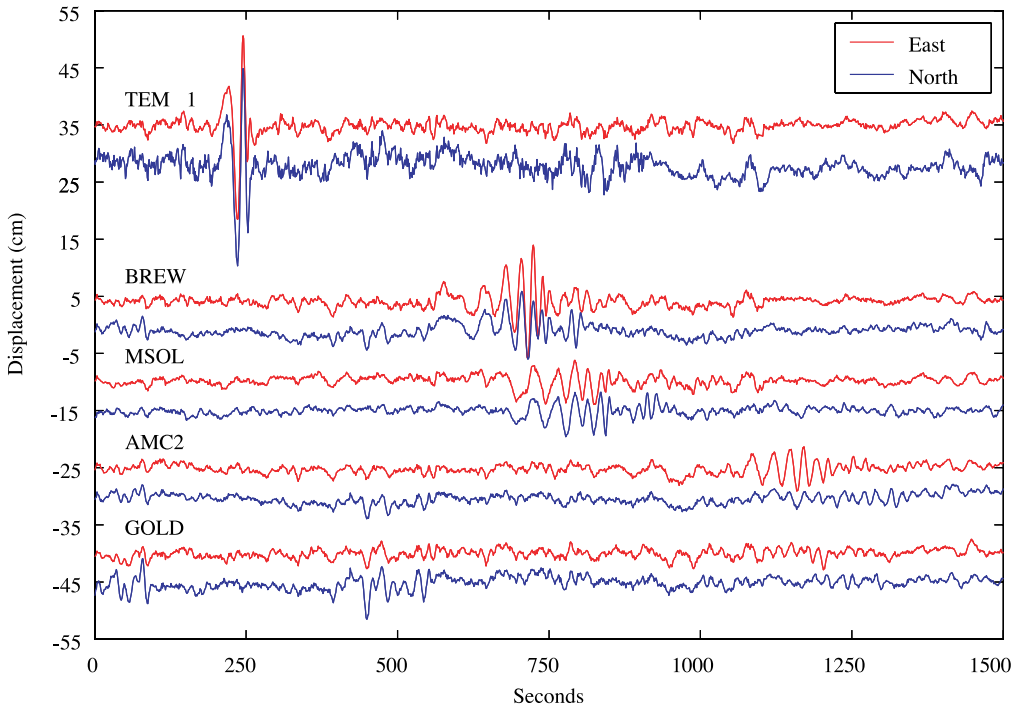


**Fig. 3.** East and north component GPS surface-wave observations at TEM1, BREW, MSOL, AMC2, and GOLD (body waves are not apparent). Time is relative to 3 November 2002 22:12:41 UTC. The dominantly strike-slip Denali fault earthquake mechanism favors the generation of Love waves (horizontally polarized transverse shear motion). This is consistent with the generally larger amplitudes on the components oriented closest to perpendicular to the rupture strike (e.g., the east component at MSOL). Vertical-position estimates are also available (fig. S1).

seismic array data suffered from noise enhancement associated with integration and from the limited bandwidth of most seismic instrumentation (*9*).

Another advantage to using GPS instrumentation to augment seismic arrays is cost. The cost of a geodetic-quality GPS receiver does not depend on the sample rate. All continuously operating GPS receivers in the United States could be run at 1 Hz; the only additional cost is for transmitting and archiving the data. The National Science Foundation (NSF) Earthscope initiative (*10*) proposes to add about 800 GPS receivers to the western United States. Our study strongly suggests that they be operated at 1 Hz. Finally, the resolution of high-frequency GPS has not been fully examined. It would be extremely useful to study GPS capabilities in the 1- to 10-Hz frequency band.

### References and Notes


1. P. Segall, J. L. Davis, *Annu. Rev. Earth Planet. Sci.* **25**, 301 (1997).
2. J. Zhang *et al.*, *J. Geophys. Res.* **102**, 18035 (1997).
3. A. Mao, C. Harrison, T. Dixon, *J. Geophys. Res.* **104**, 2797 (1999).
4. D. Eberhart-Phillips *et al.*, *Science*, **300**, 1113 (2003).
5. Information on materials and methods is available on *Science* Online.
6. R. Nikolaidis *et al.*, *J. Geophys. Res.*, doi: 10.1029/2001JB000329 (2001).
7. A number of stations across the western United States clipped (i.e., amplitudes exceeded the recording capabilities) with the passage of surface waves from the Denali fault earthquake. All of the Yellowstone and Utah short-period seismometers (L4C and S13s) and some broadband seismometers (CMT-40) clipped in the Yellowstone array (*11*).
8. D. P. Hill *et al.*, *Science* **260**, 1617 (1993).
9. J. Gomberg, G. Pavlis, P. Bodin, *Bull. Seismol. Soc. Am.* **89**, 1428 (2000).
10. Earthscope is a multidisciplinary NSF-funded project that includes seismology (USArray), geodesy (Plate Boundary Observatory), and borehole instrumentation (San Andreas fault at Depth). More information is available at www.earthscope.org.
11. R. Smith, personal communication.
12. The Harvard centroid moment tensor (CMT) for the Denali fault earthquake was taken from an online searchable database at www.seismology.harvard.edu/CMTsearch.html.


13. K.L. acknowledges NSF Grant EAR-0003943. G. Rosborough derived the coseismic constraints for the integration of seismic accelerations and produced the final form of Fig. 1 (Generic Mapping Tools). The International GPS Service Continuously Operating Reference Stations, Jet Propulsion Laboratory (section 335), Crustal Dynamics Data Information System, Scripps Orbits and Permanent Array Center, and UNAVCO, Inc., provided important infrastructure support for this study. C. Clarke of AeroMap U.S. provided the data from TEM1. K.L. thanks J. Freymueller, J. Ray, P. Shearer, Y. Bock, and W. Prescott for helpful discussions. Two anonymous reviewers provided helpful feedback that greatly improved the manuscript.


**Supporting Online Material**

www.sciencemag.org/cgi/content/full/1084531/DC1
Materials and Methods
Figs. S1 and S2
Table S1
References


14 March 2003; accepted 1 May 2003
Published online 15 May 2003;
10.1126/science.1083780
Include this information when citing this paper.


# Seismic Imaging of the Downwelling Indian Lithosphere Beneath Central Tibet


**Frederik Tilmann,[1]*† James Ni,[1] INDEPTH III Seismic Team[2]**



**A tomographic image of the upper mantle beneath central Tibet from INDEPTH data has revealed a subvertical high-velocity zone from ~100- to ~400-kilometers depth, located approximately south of the Bangong-Nujiang Suture. We interpret this zone to be downwelling Indian mantle lithosphere. This additional lithosphere would account for the total amount of shortening in the Himalayas and Tibet. A consequence of this downwelling would be a deficit of asthenosphere, which should be balanced by an upwelling counterflow, and thus could explain the presence of warm mantle beneath north-central Tibet.**


The Himalayan Tibetan orogen provides one of the best natural laboratories to study the complex ways in which continents respond to collision. This orogen was created by collision and subsequent penetration of India into Asia starting sometime between 50 and 65 million years ago (Ma) (*1*). The mode of convergence (currently at 4 cm/year) has been attributed to (i) escape tectonics, the east-to-southeast–directed lateral extrusion of Tibet along strike-slip faults (Fig. 1); (ii) distributed thickening of the Tibetan crust and mantle lithosphere; and (iii) underthrusting of the Indian lithosphere along a detachment and imbricate Himalayan thrust sheets (*2*). The more or less uniform elevation of the plateau of ~5 km hides marked differences in the structure of the mantle beneath. Various surface-wave studies (*3*–*6*) and observations of $P_n$ and $S_n$ (*7*, *8*) show that immediately beneath the 70- to 80-km-thick crust, fast and presumably cold and strong mantle prevails in southern Tibet, whereas slower, presumably warmer and weaker mantle, with increased attenuation and a reduced *S*-wave velocity gradient below the Moho, is found north of 32°N (about ±0.5°), near the Bangong-Nujiang Suture (BNS) (for the purpose of this paper, northern and southern Tibet are defined to be separated by this boundary) (Fig. 1A). The mantle heterogeneities are generally interpreted as evidence of underthrusting of Indian lithosphere to near the middle of the plateau. However, a simple consideration of either the total convergence since the collision of about 1800 to 2500 km estimated from magnetic anomalies (*9*) or an estimate of the minimal shortening in the Himalayan fold-thrust belts of 500 to 700 km (*9*, *10*) or even a simple-minded extrapolation of the present-day convergence of ~15 mm/year between India and the Indus Yarlung Suture (*11*) would put an undeformed Indian mantle lithosphere entirely or partially into the region of warmer mantle beneath northern Tibet. These estimates imply that either the underthrusted Indian lithosphere has shortened substantially since collision, or additional lithosphere exists in the upper mantle beneath central Tibet.

As part of the INDEPTH III (I3) multidisciplinary project, a quasilinear array of ~40 broadband and intermediate-band stations recorded teleseismic and regional earthquakes from July 1998 to June 1999 (Fig. 1B). These data are supplemented by six stations from the 1994 INDEPTH II (I2) deployment, which approximately extend along the line of the I3 stations, and the permanent CDSN station LSA. Here, we present a tomographic image along the strike of the combined array, about north-northwest–south-southeast from 29°N to 33.5°N, centered at ~90°E. We assumed that there is no large variation of the mantle structure in the east-west direction because in the study region both major geologic structures and the regions delineated by $P_n$ and $S_n$ propagation studies are nearly east-west trending. We only used earthquakes whose backazimuths differed by no more than 30° from the average strike of the I2 and I3 arrays (153°) or that have very steep incidence angles in order to reduce bias due to the possible three-dimensionality of the structure. Altogether 32 out of 98 picked earthquakes during I2 and 36 out of 120 picked earthquakes during I3 fulfilled this criterion and yielded data of sufficient quality for further analysis (*12*).

The preferred model resulting from the tomographic inversion (Fig. 2) can resolve structures between 29°N and 33.5°N and between depths of ~100 to 400 km, and has a resolving power of ~60 km horizontally and ~100 km vertically (*13*). The velocity model is represen-


[1]Department of Physics, New Mexico State University, Las Cruces, NM 88003, USA. [2]INDEPTH III Seismic Team: T. Hearn, Y. S. Ma, R. Rapine (New Mexico State Univ.), R. Kind, J. Mechie, J. Saul (GFZ Potsdam), S. Haines, S. Klemperer (Stanford Univ.), L. Brown, P. Pananont, A. Ross (Cornell Univ.), K. D. Nelson (Syracuse Univ.), J. Guo, W. Zhao (Chinese Academy of Geological Sciences)

*Present address: Department of Earth Sciences, Cambridge University, Cambridge CB3 0EZ, UK.
†To whom correspondence should be addressed. E-mail: tilmann@esc.cam.ac.uk